Acta Crystallographica Section A
Foundations of Crystallography
ISSN 0108-7673

Received 6 February 2001
Accepted 21 May 2001

Systematic intensity errors caused by spectral truncation: origin and remedy

A. T. H. Lenstra,* J. F. J. Van Loock, B. Rousseau and S. T. Maes

Department of Chemistry, University of Antwerp (UIA), Universiteitsplein 1, B-2610 Antwerpen, Belgium. Correspondence e-mail: lenstra@uia.ua.ac.be

The wavelength dispersion of graphite(002)-monochromated X-ray beams has been determined for a Cu, a Mo and an Rh tube. The observed values for $\Delta\lambda/\lambda$ were 0.03, 0.14 and 0.16, respectively. The severe reduction in monochromaticity as a function of wavelength is determined by the absorption coefficient μ of the monochromator. μ(monochromator) varies with λ^3. For an Si monochromator with its much larger absorption coefficient, $\Delta\lambda/\lambda$ values of 0.03 were found, regardless of the X-ray tube. This value matches a beam divergence defined by the size of the focus and of the crystal. This holds as long as the monochromator acts as a mirror, *i.e.* μ(monochromator) is large. In addition to monochromaticity, homogeneity of the X-ray beam is also an important factor. For this aspect the mosaicity of the monochromator is vital. In cases like Si, in which mosaicity is practically absent, the reflected X-ray beam shows an intensity distribution equal to the mass projection of the filament on the anode. Smearing by mosaicity generates a homogeneous beam. This makes a graphite monochromator attractive in spite of its poor performance as a monochromator for $\lambda < 1$ Å. This choice means that scan-angle-induced spectral truncation errors are here to stay. These systematic intensity errors can be taken into account after measurement by a software correction based on the real beam spectrum and the applied measuring mode. A spectral modeling routine is proposed, which is applied on the graphite-monochromated Mo $K\alpha$ beam. Both elements in that spectrum, *i.e.* characteristic α_1 and α_2 emission lines and the *Bremsstrahlung*, were analyzed using the 6,3,18 reflection of Al_2O_3 (s = 1.2 Å^{-1}). The spectral information obtained was used to calculate the truncation errors for intensities measured in an $\omega/2\theta$ scan mode. The results underline the correctness of previous work on the structure of $NiSO_4{\cdot}6H_2O$ [Rousseau, Maes & Lenstra (2000). *Acta Cryst.* A**56**, 300–307].

1. Introduction

Monochromatic radiation is used generally for diffraction experiments. At our institute, X-rays are generated using sealed X-ray tubes. The primary radiation is polychromatic with characteristic emission lines superimposed upon the white continuum. A pyrolytic graphite crystal (UCAR-ZYA) with a mosaicity of 0.4 (1)° full width at half-maximum (FWHM) in its rocking curve serves as monochromator. The wavelength window $\Delta\lambda$ typically present in the monochromated X-ray beam is an important element in the anatomy of a Bragg reflection. The reflection shape is determined by the mosaicity of the crystal, the size of the focal spot and the wavelength dispersion. These three elements define the size of the reflections along ω, θ and 2θ, respectively (Keulen, 1969). These elements can be observed using the so-called $\omega/2\theta$ plot (Mathieson & Stevenson, 1996). The step from the point detector to an area detector has been discussed by Duisenberg (1998).

When we differentiate Bragg's law, $2d\sin\theta = \lambda$, we find $\Delta\theta = (\Delta\lambda/\lambda)\tan\theta$. This relation links the reflection width $\Delta\theta$ to the wavelength dispersion $\Delta\lambda/\lambda$. This dispersion parallels an $\omega/2\theta$ scan direction. The finite value of $\Delta\lambda/\lambda$ is included in the measuring strategy *via* the scan angle a, which is given by $a = [a_o + (\Delta\lambda/\lambda)(360/2\pi)\tan\theta]^\circ$. The scan width a ensures that each individual intensity is properly integrated over the complete spectrum present in the crystallographic X-ray beam. A review on the interpretation of single-crystal diffraction intensities has been presented by Blessing (1987).

While analyzing background intensities, upon which the Bragg reflections are superimposed, Maes *et al.* (1998) have reported a $\Delta\lambda/\lambda$ value of 0.14 for the combination Mo $K\alpha$/graphite(002) on a CAD4 diffractometer. Given this $\Delta\lambda/\lambda$ value, an intensity integration requires a scan width of $(a_o + 8.0\tan\theta)^\circ$. This width becomes so large that individual intensities cannot be observed along a reciprocal axis. Those intensities can only be measured separately when the applied scan angle underestimates the real $\Delta\lambda/\lambda$ value. This delib-

erate choice introduces spectral truncation errors. Their consequences have been analyzed by Rousseau *et al.* (2000). Atomic temperature factors were shown to increase by ∼0.05 and 0.22 Å^2 for measurements with tube voltages of 50 and 25 kV, respectively. This structural bias is seldom recognized. A spectral analysis was presented by Denne (1977). His corrections were severely criticized by *e.g.* Eisenstein & Hirshfeld (1983). [See also a follow-up by Mathieson (1989).]

The real errors are much larger than those described by Denne (1977) because the spectral truncation error is not determined by the $K\alpha$ emission lines but by the white continuum. This explains the impact of the tube voltage on the magnitude of the intensity truncation. At 0.9 Å^{-1}, the systematic intensity error is ∼10% at 50 kV and ∼30% at 25 kV. Similar values have been reported by Hirshfeld & Hope (1980) and Destro & Marsh (1987, 1993).

In §2, we analyze the performance of a graphite monochromator in combination with X-ray beams generated with fine-focus tubes with a Cu, an Mo and an Rh anode. Measurements were made with a tube tension of 50 kV. X-ray absorption, which varies roughly with λ^3, determines the variation in the wavelength dispersion, $\Delta\lambda/\lambda = (\lambda_{max} - \lambda_{min})/\lambda_{ave}$. The impact on the beam spectrum by other elements, such as additional collimation, monochromator positioning and the selected energy window in the counting chain, are investigated.

A high X-ray absorption by the monochromator leads to a minimum $\Delta\lambda/\lambda$ value. Therefore we replace in §3 the graphite monochromator by a silicon one. We find values of 0.03 for the wavelength dispersion. Unfortunately, Si monochromators are practically non-mosaic. In the absence of the mosaicity-related intensity smearing, we find that the Si(111)-monochromated X-ray beams have a very inhomogeneous intensity distribution. This makes those beams highly unattractive for diffraction studies.

An experimental set-up, in which intensity truncation errors can be avoided during data collection, appears to be impossible except at synchrotron facilities. The local laboratory equipment will therefore always produce high-resolution data sets ($0 < s < 1$ Å^{-1}) with large intensity errors caused by spectral truncation. These systematic intensity errors can be eliminated by an *a posteriori* correction, which combines the actual beam spectrum with the applied measuring mode. The beam spectrum contains the α_1 and α_2 emission lines on the one hand and a *Bremsstrahlung* component on the other hand. For the spectral analysis of a graphite-monochromated Mo $K\alpha$ beam, we used a spherical Al_2O_3 crystal; intensity profiles of its 6,3,18 reflection ($s = 1.2$ Å^{-1}) were employed.

In §4.1, we concentrate our efforts on the characteristic emission lines of Mo $K\alpha$. A 3.1° scan along $\omega/2\theta$ served to measure the necessary details. The model description includes: (i) two Lorentzian distributions for the α_1 and the α_2 lines; (ii) a reflection width determined by the beam divergence and the crystal radius. The positional uncertainties affecting the reproducibility of the profile scans are examined in detail.

In §4.2, we examine the white continuum component in the 6,3,18 profile. Scans over 21° in ω (or θ) provided the experimental evidence. We modeled the *Bremsstrahlung* using a ten-parameter expression.

In §5, we calculate the systematic intensity errors from the beam spectrum and the scan angle for measurements along the $\omega/2\theta$ scan direction. The results fit perfectly with those presented previously (Rousseau *et al.*, 2000) on the relation between model imperfection and truncation errors in the case of $NiSO_4{\cdot}6H_2O$. To check the impact of truncation on the X-ray model, we present an analysis based on simulated data.

Conclusions are drawn in §6.

2. Graphite monochromator: its impact on the reflection shape

For our experiments we used an Enraf–Nonius CAD4 diffractometer. The details regarding its geometry are shown in Fig. 1. A sealed tube was used to generate the X-rays, which were monochromated by a pyrolytic graphite crystal (UCAR-ZYA) with a mosaicity of 0.4 (1)° FWHM in its rocking curve. The monochromator dimensions are 12 × 6 × 2 mm. We analyzed the spectral composition of the monochromated X-ray beams obtained with fine-focus tubes with an Rh, an Mo and a Cu anode. The monochromator angle θ_m was set at 5.2° (Rh $K\alpha$; 0.61 Å), 6.1° (Mo $K\alpha$; 0.71 Å) and 13.3° (Cu $K\alpha$; 1.54 Å). The collimation of the CAD4 equipment prevented, even at small monochromator angles, the irradiation of the crystal to be analyzed by X-rays coming directly from the tube's focus. In each experiment, the detection chain was adjusted to the relevant photon energies of 20, 17.5 and 8.0 keV. The outcome of a wavelength-dispersive profile analysis depends obviously on the selected setting of the detector unit. Fortunately, it is easy to measure the response function of the detector by analyzing the tube spectrum itself. Details are given in Appendix *A*.

Spectra were recorded using an Si crystal (0.4 × 0.4 × 0.4 mm) as an analyzer. The Si mosaicity was negligible; we measured a profile width of 0.02° FWHM in ω. Low- and high-order Si reflections were measured in an $\omega/2\theta$ scan mode. This scan direction parallels the wavelength axis. The width of each profile scan was set at 21° in ω. This large scan range allowed us to observe the coherent Bragg reflection superimposed upon the incoherently scattered background. The background signal itself is not monochromatic in contrast

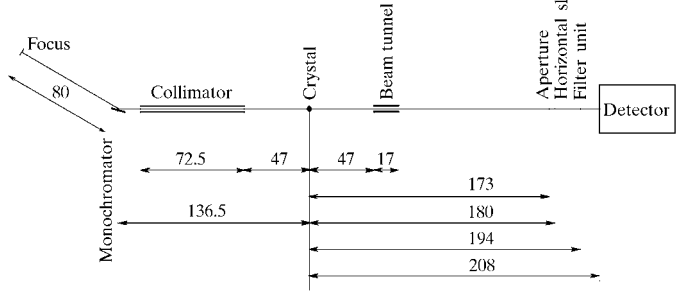

Figure 1
Relevant dimensions (in mm) of the CAD4 diffractometer.

to the coherent reflection profile. Within that profile, Bragg's law ($2d \sin\theta = \lambda$) links the scattering angle directly to the relevant wavelength. A typical result of the measurements is shown in Fig. 2.

The Si($\bar{1}3\bar{3}$) profile, observed with Cu $K\alpha$, begins at $\theta = 37.9°$ and ends at a Bragg angle of 39.1°. This corresponds to wavelength limits of 1.52 and 1.56 Å. Consequently, the monochromated Cu $K\alpha$ beam shows a wavelength dispersion $(\lambda_{max} - \lambda_{min})/\lambda_{ave}$ of 0.03. Optical beam tracking suffices to link the instrumental geometry with $\Delta\lambda/\lambda$. This is illustrated in Fig. 3. The instrumental geometry, the size of the Si crystal and the dimensions of the focal spot determine the angular dispersion $\Delta\theta$, which matches the observed value of $\Delta\lambda/\lambda$. In this construction, we assume that the monochromator acts as an X-ray mirror, *i.e.* the coherent scattering of the monochromator is restricted to its surface. Under these conditions we find, for the fine-focus Cu tube (see Fig. 3), the wavelength limits of 1.52 and 1.56 Å.

As we see in Fig. 2, the reflection profiles for Rh $K\alpha$ and Mo $K\alpha$ are quite asymmetric. The Mo profile of Si($\bar{1}3\bar{3}$) suggests, *via* its Bragg angles (see Fig. 2), values of 0.69 and 0.79 Å for λ_{min} and λ_{max}. The analogous Rh profile leads to wavelength limits of 0.59 and 0.69 Å. Instead of a $\Delta\lambda/\lambda$ value of 0.03 typical for Cu $K\alpha$, we now find wavelength dispersions of 0.14 and 0.16 for Mo and Rh, respectively. The skewness of the reflection profiles leads to geometrical mean wavelength values of 0.74 and 0.64 Å, which are 0.03 Å larger than the $K\alpha$ wavelengths of 0.71 and 0.61 Å. The asymmetry in the Mo and Rh profiles is incompatible with the monochromator mosaicity. That property causes a symmetric wavelength smearing in line with the Cu profile shown in Fig. 2.

To verify the wavelength assignment within the Mo $K\alpha$ related Si($\bar{1}3\bar{3}$) profile, we reanalyzed that reflection, inserting metal absorption foils between the Si analyzer and the NaI detector. The reflection profiles observed with and without a Y absorption foil are depicted in Fig. 4(*a*). The absorption edge at $\lambda = 0.728$ Å is clearly visible. At this point, we observe a significant shift in the X-ray transmission within the coherent Bragg reflection. The transmission changes from 0.34 ($\lambda < \lambda_{abs}$) to 0.85 ($\lambda > \lambda_{abs}$). The coherent, and thus monochromatic, Bragg reflection is superimposed upon a polychromatic background. Here the X-ray transmission through the Y foil is a weighted average between the characteristic $K\alpha$ emission (0.34) and the white continuum (with a transmission of 0.85 for $\lambda > \lambda_{abs}$). This explains the transmission returning to ~0.45 beyond $\lambda = 0.79$ Å, because at this point the Bragg intensity becomes zero and the profile intensity is determined by the incoherently scattered background. When we replace the Y foil by a Zr foil ($\lambda_{abs} = 0.688$ Å), we do not see any abrupt changes in the foil transmission. Thus, wavelengths $\lambda < 0.688$ Å are not detectable in the reflection profile, whereas $\lambda > 0.728$ Å are easily observed.

Let us assume that the graphite-monochromated Mo $K\alpha$ beam contains only two wavelengths, *viz* the characteristic Mo $K\alpha$ radiation ($\lambda = 0.71$ Å and a Y transmission of 0.34) and a white-continuum-induced component ($\lambda = 0.73$ Å and a foil transmission of 0.85). In the absence of a foil, the observed intensity $I = I_1 + I_2$, where I_1 is the beam intensity for $\lambda = 0.71$ Å and I_2 is the beam intensity for $\lambda = 0.73$ Å. Insertion of the absorption foil leads to an intensity $I' = 0.34I_1 + 0.85I_2$. This enables us to reconstruct an I_1 and an I_2 profile. This is depicted in Fig. 4(*b*). About 15% of the background signal is determined by I_2, *i.e.* $\lambda > 0.728$ Å. The intensities of the I_1- and I_2-related parts of the Bragg reflection lead to a similar estimate of 12%. This illustrates clearly the importance of the tube's white continuum as a component in the monochromated Mo $K\alpha$ beam.

At $\lambda = 0.35$ Å, we observe a small, but significant, peak in the Si($\bar{1}3\bar{3}$) profile. Its height is ~1% of the maximum signal in the Bragg reflection. The peak corresponds to Si($\bar{1}3\bar{3}$) for $\lambda/2$. This wavelength is present in the monochromated X-ray beam as the coherently scattered graphite (004) reflection. When we reduce the tube tension from 50 to 30 kV, the profile peak for $\lambda/2$ disappears, because the minimum wavelength in the *Bremsstrahlung* shifts from 0.248 to 0.413 Å.

Accidentally, the Y absorption at $\lambda = 0.35$ Å is equal to the absorption at $\lambda = 0.73$ Å. This explains why the $\lambda/2$-determined maximum disappears in the I_1 profile and returns fully in the I_2 profile.

Traditionally (see *e.g.* Arndt & Wonacott, 1977), two elements are used to explain the impact of a crystalline monochromator, *viz* (i) the coherent scattering of the monochromator is restricted to its surface, (ii) the Bragg angle is smeared by the mosaicity of the monochromator.

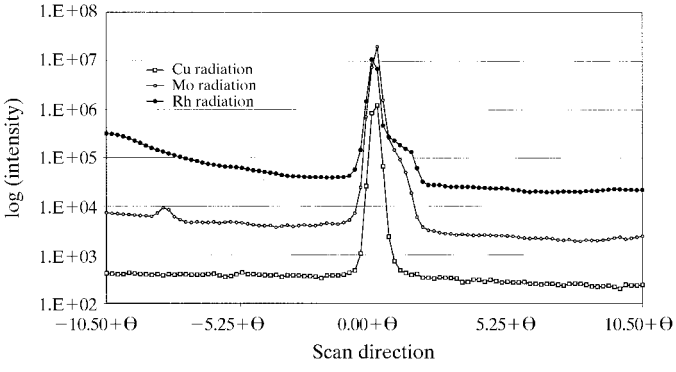

Figure 2
The Si($\bar{1}3\bar{3}$) reflection profile measured with graphite(002)-monochromated radiation. The relevant Bragg angles θ are 14.2, 16.6 and 38.2° for Rh, Mo and Cu radiation, respectively. For clarity the reflection profiles are shifted along the intensity axis.

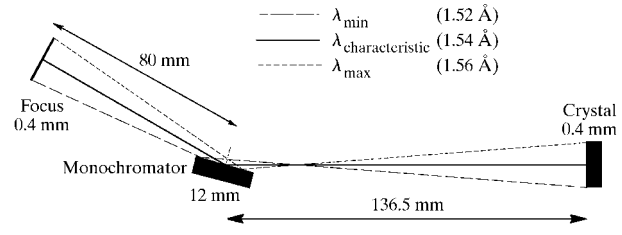

Figure 3
Optical beam tracking links a wavelength dispersion of 0.03 with a beam divergence $\Delta\theta$ determined by the size of the crystal and the dimensions of the focal spot.

To understand the Mo and the Rh measurement, depicted in Fig. 2, we have to include the monochromator's X-ray absorption in our logic. The mass absorption coefficient μ/ρ of graphite is 0.460 $m^2\ kg^{-1}$ for Cu $K\alpha$; this reduces to 0.0625 and 0.0469 $m^2\ kg^{-1}$ for Mo $K\alpha$ and Rh $K\alpha$, respectively. This decrease in μ by an order of magnitude increases the *infinite* thickness of the monochromator. In practice, the infinite thickness is taken equal to $6/\mu$. This optical path reduces the transmitted X-ray intensity to a level smaller than 1% of the original intensity. This logic is used to calculate *e.g.* the required thickness of a β filter. The scattering by layers deeper inside the monochromator causes additional freedom in the range of available Bragg angles. This is illustrated in Fig. 5.

During the X-ray alignment, one aims at the highest possible intensity in the monochromated X-ray beam. This leads to a monochromator position in which the characteristic radiation is scattered as close to the monochromator surface as possible yielding a minimum absorption for $K\alpha$. From Fig. 5, we learn that this leads to a strong preference for wavelengths greater than $K\alpha$ in the monochromated beam *via* reflection at deeper layers. The maximum wavelength of 0.77 Å in the monochromated X-ray beam is defined by the 12 mm length of the monochromator. In our experiments, we used a second generation of the monochromator device. Here the graphite crystal is embedded in a metal frame. Therefore, the monochromator length of 12 mm is well defined. In addition, the complications, which were caused by the X-ray transmission *via* the side faces of the graphite crystal in the original series of monochromators, are non-existent in the current models. The length of the monochromator allows X-rays to arrive at the Si analyzer after an optical path of slightly over 12 mm through graphite. This path leads for $\lambda \simeq$ Mo $K\alpha$ to a loss of 70% of the initial intensity. In the original tube spectrum, the intensity I at λ = 0.77 Å is about 3% of the Mo $K\alpha$ intensity when we operate the X-ray tube at 50 kV (Maes, 1997). In Fig. 2, I at λ = 0.77 Å is 1% of I(Mo $K\alpha$). Thus, absorption bridges the gap between the tube spectrum and its graphite-monochromated counterpart. The beam-tracking procedure shown in Fig. 5 suggests a $\Delta\lambda/\lambda$ value of 0.09 for a point focus. Smearing *via* the size of the focus (we used 0.4 × 0.8 mm *via* a take-off angle of 6°) and the mosaicity increases $\Delta\lambda$ symmetrically to a minimum and a maximum wavelength of 0.69 and 0.79 Å, respectively. During the spectral analysis of the monochromated Mo $K\alpha$ beam, we measured the reflection profiles with an energy window of 170 V in the detector chain. In an effort to reduce $\Delta\lambda/\lambda$ we decreased this window from 170 to 25 V. We hoped that this would lead to an increased selectivity towards the Mo $K\alpha$ photons. The decrease in energy window reduced the observed intensity to ∼20% of its original value. This drop in intensity turned out to be wavelength independent. Thus, the wavelength dispersion $\Delta\lambda/\lambda$ in the graphite-monochromated Mo $K\alpha$ beam was in practice not affected by the window setting of the detector. The geometrical mean wavelength in a graphite-monochromated Mo $K\alpha$ beam is 0.74 Å. The beam spectrum (see Figs. 2 and 4) shows an intensity tail favoring λ > 0.71 Å. As stated above, this asymmetry in the spectral distribution is connected to the monochromator alignment, in which a maximum beam intensity is pursued. By increasing the height of the monochromator, the spectral asymmetry can be reversed. After a full alignment of the equipment, we increased the monochromator height by 0.15 mm without changing the monochromator angle. The adjustment in the monochromator height halved the intensity of the Mo $K\alpha$ emission line by monochromator absorption. The beam spectrum showed an intensity tail in the direction λ < 0.71 Å. The presence of these short wavelengths was verified by the introduction of a Zr foil. The absorption edge at 0.688 Å was clearly visible, but only in the beam generated with the monochromator in the elevated

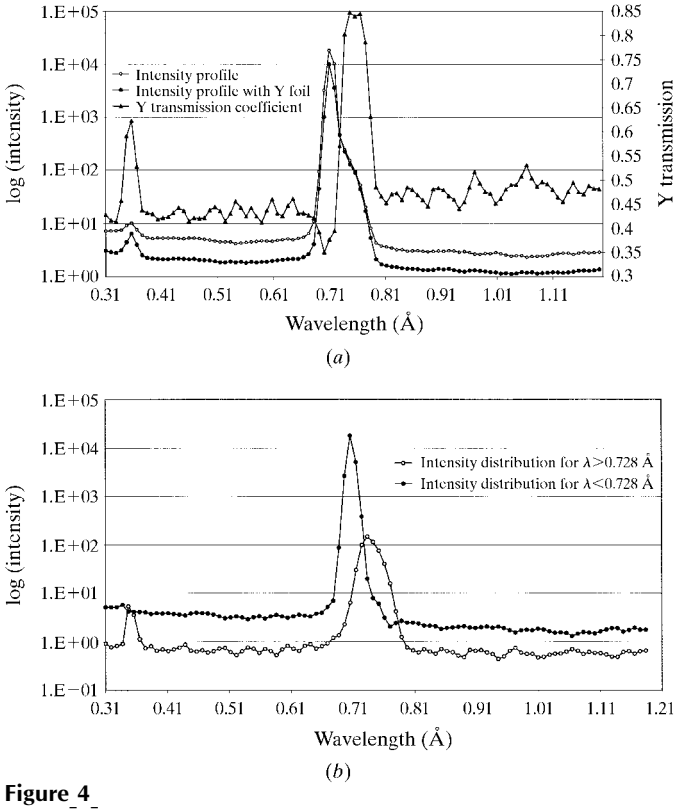

Figure 4
(*a*) Si($\bar{1}3\bar{3}$) reflection profiles observed with graphite(002)-monochromated Mo $K\alpha$ radiation in the presence and in the absence of a Y absorption foil. The foil transmission changes from 0.34 to 0.85 at the Y absorption edge (0.728 Å). (*b*) The original Si($\bar{1}3\bar{3}$) intensity distribution divided into its intensity components I_1 with λ < 0.728 Å and I_2 with λ > 0.728 Å.

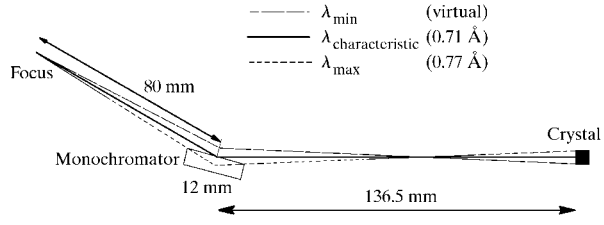

Figure 5
The asymmetry in $\Delta\lambda$ is determined by the X-ray absorption of the monochromator. When the monochromator geometry is tailored to λ = 0.71 Å, we find a λ_{max} value of 0.77 Å. This value is dictated by the 12 mm length of the graphite monochromator.

position. The elevation of the monochromator shifts the wavelength window $\Delta\lambda$ towards smaller wavelengths; unfortunately, the wavelength dispersion of $\Delta\lambda/0.71$ Å remains unaffected. In a combination with the Zr foil, it is possible to reduce $\Delta\lambda$, because it allows the elimination of $I(\lambda)$ with $\lambda < 0.688$ Å. The increase in the height of the monochromator is accompanied by the expense of ~50% of I(Mo $K\alpha$). The additional use of a Zr foil costs another 50% of the remaining beam intensity. Therefore, a 'monochromatic' experiment on the equipment in the laboratory is possible when we are willing to give up ~75% of the original beam intensity. For routine measurements, this is an unattractive proposition. For monochromatic data, an experiment based on balanced filters or on balanced tubes (Rousseau *et al.*, 2000) should (in our opinion) be preferred.

The angular divergence of the radiation was reduced on our instrument by inserting an additional collimator between the focus and the monochromator. We used a Cu cylinder with a length of 20 mm and an inner diameter of 0.5 mm, *i.e.* an opening with the size of the focus and of the crystal. This collimator helps to control $\Delta\lambda/\lambda$ *via* a limitation in the scattering volume of the monochromator. The Mo $K\alpha$ beam intensity was reduced to 30% of its uncollimated value. The wavelength dispersion decreased from 0.14 to 0.09, which is still unattractively large. Further investigations were not performed in view of the poor cost-to-benefit ratio.

3. Si(111) monochromator

The wavelength dispersions of 0.03, 0.14 and 0.16 for the monochromated Cu $K\alpha$, Mo $K\alpha$ and Rh $K\alpha$ beams are determined by the X-ray absorption properties of the graphite monochromator. The best $\Delta\lambda/\lambda$ value of 0.03 is connected to the largest value for μ. When we replace the graphite monochromator by a silicon crystal, the relevant mass absorption coefficients increase by one order of magnitude. For Cu, Mo and Rh, we obtain μ/ρ values of 6.06, 0.644 and 0.425 $m^2\ kg^{-1}$. Since ρ(graphite) = 2.267 Mg m^{-3} is almost equal to ρ(Si) = 2.329 Mg m^{-3}, μ(graphite; Cu $K\alpha$) $\simeq$ μ(Si; Rh $K\alpha$) and therefore a $\Delta\lambda/\lambda$ value of 0.03 can be expected for (Si, Rh $K\alpha$).

The Si($\bar{1}3\bar{3}$) profiles observed with an Si(111)-monochromated X-ray beam are shown in Fig. 6. The monochromator angles θ_m were 14.2, 6.5 and 5.6° for Cu, Mo and Rh, respectively. Therefore, θ_m(Si) is almost equal to θ_m(graphite). In all three profiles, we find an experimental value for $\Delta\lambda/\lambda$ of 0.03. This value agrees well with the beam tracking model illustrated in Fig. 3.

In general, the spectral quality of the Si(111)-monochromated X-ray beams has to be preferred over the standard beams obtained *via* graphite(002). The latter approach results in quite asymmetric reflection profiles with a wavelength dispersion of 0.14 for Mo $K\alpha$. This reduces to 0.03 for the combination Si/Mo $K\alpha$ with the additional advantage that this spectral profile (see Fig. 6) is symmetric around Mo $K\alpha$. This is the positive consequence of increased monochromator absorption. The negative side is the reduction in the intensity of the monochromated X-ray beam. For Mo, the intensity decreases by one order of magnitude. This is easily understood, because the increase in μ lowers the scattering volume of the monochromator by its impact on the *infinite* thickness.

The practical absence of mosaicity in the Si monochromator creates, unfortunately, an inhomogeneous intensity distribution in the monochromated X-ray beam. We measured the intensity distribution in that beam by placing a metal plate with a small hole of 25 µm at the position normally occupied by the crystal on the diffractometer. The hole could be shifted in the plane of the detector and perpendicular to it. Parallel to the rotation axis of the monochromator, *i.e.* in the plane of the CAD4 detector movement, we observed a homogeneous X-ray intensity over a range that exceeds the 0.8 mm length of the focal spot as determined by the 8 mm length of the filament and the take-off angle of 6° for the X-ray tube.

Perpendicular to the detector plane, *i.e.* along the direction of the wavelength dispersion in the monochromator reflection, we measured strong intensity variations. Three observed intensity profiles are summarized in Fig. 7. A fine-focus Mo tube produces, along the monochromator-induced dispersion axis, a homogeneous beam intensity over a range of ~ 0.8 mm

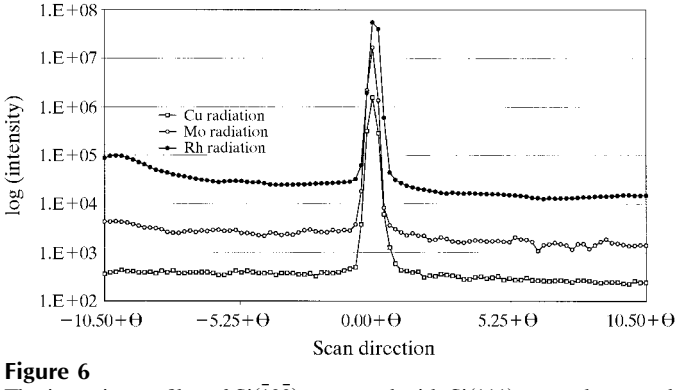

Figure 6
The intensity profiles of Si($\bar{1}3\bar{3}$) measured with Si(111)-monochromated radiation. The reflection profiles for Rh, Mo and Cu have been shifted along the intensity axis for clarity. The relevant θ values are 14.2, 16.6 and 38.2° for Rh, Mo and Cu, respectively. The width of 2° for the Si($\bar{1}3\bar{3}$) reflection is practically wavelength independent.

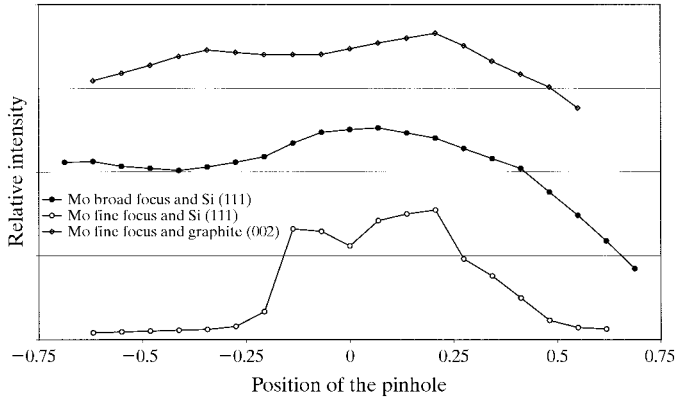

Figure 7
The intensity distribution along the instrumental Z axis, *i.e.* along the direction of the wavelength dispersion in the monochromator reflection.

provided that we use the graphite monochromator. In the absence of mosaicity, the beam diameter shrinks considerably to a size of less than 0.6 mm. Within that beam, we find two intensity maxima. They are separated by 0.4 mm, which equals the diameter of the tube's filament. The intensity distribution itself is practically equal to the mass projection of the filament on the tube's anode. In the absence of mosaicity, the initial intensity distribution emitted by the tube's focus is preserved. The asymmetry between the upper and lower halves of the intensity profile is related to the $\alpha_1-\alpha_2$ splitting. This is illustrated in Fig. 8, where we examine the intensity profile of the Si(0,0,16) reflection observed with Rh $K\alpha$ radiation monochromated with Si(111). The reflection is centered at 1.47 Å^{-1}. The upper part of the X-ray beam (*i.e.* the positive displacements along Z in Fig. 7) produces the expected α_1:α_2 intensity ratio of 2:1. Using the bottom half of the same X-ray beam, we find a value of 10 for α_1/α_2. Note that in both cases $I(\alpha_1)$ shows the same intensity. This observation was made with an instrumental geometry that was acceptable for the instrumental alignment routine.

To measure reflection intensities with an inhomogeneous intensity distribution in the X-ray beam is not sensible. To improve this aspect of the beam quality, we repeated our analysis with a broad-focus Mo tube. Its filament size was 2 × 12 mm. Owing to the increased filament diameter, we arrive at an almost homogeneous beam (see Fig. 7). However, this does not make the broad-focus tube an attractive diffraction tool. The increase in the focal spot (2 × 1.2 mm) leads to an increase in the beam divergence $\Delta\theta$ which leads automatically to a larger wavelength dispersion. This is illustrated in Fig. 9. The fine-focus tube (focal spot 0.4 × 0.8 mm) leads to a $\Delta\lambda/\lambda$ value of 0.03, which increases to 0.09 for the broad-focus tube.

In order to speed up data collection, high-intensity X-ray beams are necessary. Such beams can be produced in the home laboratory with a rotating-anode device. A maximum beam intensity requires the use of a large filament. Our $\Delta\lambda/\lambda$ analysis explains that the expected profit in time is easily cancelled out by the increase in the size of each reflection. For a point detector, the scan range per reflection is given by $[a_0 + (\Delta\lambda/\lambda)(360/2\pi)\tan\theta]^\circ$. At $\theta = 45^\circ$, this leads to a scan angle of $(a_0 + 1.72)^\circ$ for the combination fine-focus Mo-tube/Si-monochromator. This scan range expands to $(a_0 + 5.73)^\circ$ when we use a broad-focus Mo tube with the same monochromator.

4. Modeling the beam spectrum

The CAD4 diffractometer has a perpendicular monochromator geometry and as a consequence the reflecting net planes of the analyzer crystal are positioned perpendicular to the net planes of the monochromator. This has the advantage that the spectral dispersion $\Delta\lambda$ is symmetric around $\theta = 0^\circ$ (Blessing, 1987; Ryan, 1986).

To analyze the beam spectrum, we decided to use a spherical crystal. Such crystals of α-corundum (Al_2O_3; space group $R\bar{3}c$; $a = 4.761$, $c = 12.996$ Å) with a diameter of 0.300 (3) mm have been distributed by Enraf–Nonius as a follow-up of the ruby spheres distributed by the National Research Council of Canada during the IUCr meeting in Ottawa in 1981. The small mosaicity minimized the effects of wavelength smearing in the Bragg reflections to be used in our wavelength-dispersive measurements. For our spectral analysis, we selected the 6,3,18 reflection, which we measured with a graphite-monochromated Mo $K\alpha$ beam. With $\Delta\lambda/\lambda = 0.14$, the required angular width in the profile scan is equal to $(a_0 + 8.02\tan\theta)^\circ$. For the selected reflection at 1.2 Å^{-1}, an $\omega/2\theta$ scan over 21° shows a clear α_1, α_2 split. However, only a very limited number of steps in the total profile provides information on the Mo $K\alpha$ doublet. In a previous analysis (Rousseau *et al.*, 2000), we used this information to summarize the characteristic emission lines in two Lorentzian expressions. We found 0.00227 and 0.00089 Å for the FWHM of α_1 and α_2. The correct values are 0.00029 and 0.00032 Å (Compton & Allison, 1935).

To obtain an adequate description of the Mo $K\alpha$ emission lines we decided to measure the 6,3,18 profile in two steps, *viz*: (i) a limited scan width of 3.1° was used to zoom in on the emission lines; during the data collection, λ was taken equal to

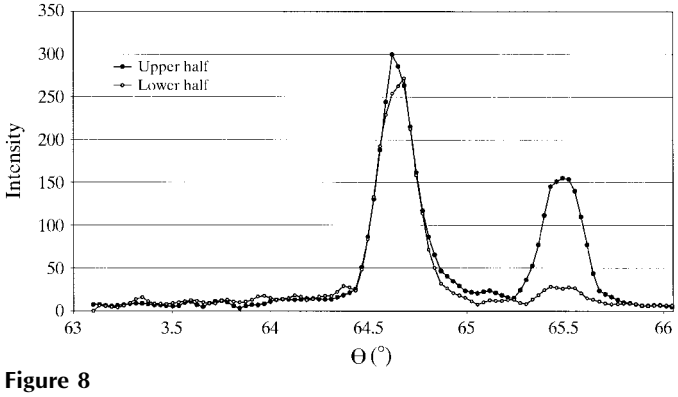

Figure 8
The Si(0,0,16) reflection measured with Si(111)-monochromated Rh $K\alpha$ radiation. Note the difference in the intensity patterns observed using selectively the lower and the upper halves of the monochromated X-ray beam.

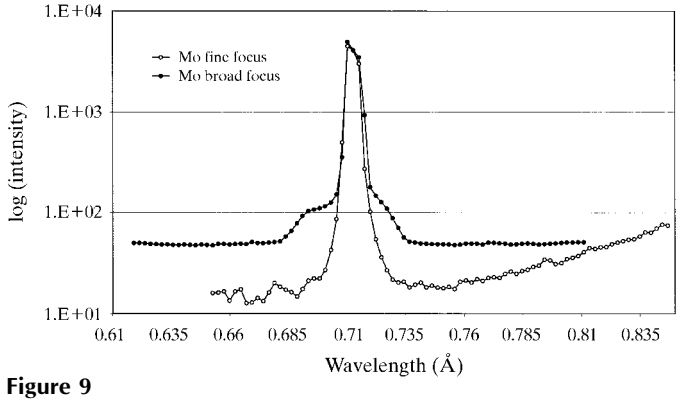

Figure 9
The Si(0,0,12) reflection profiles illustrate the increase in wavelength dispersion when an Mo fine-focus tube is replaced by an Mo broad-focus tube. The different behavior in the background intensity is caused by radiation leaking away from the monochromator in the experiment with the Mo fine-focus tube.

$(\alpha_1 + \alpha_2)/2$; (ii) a 21° wide-angle scan was employed to measure the complete reflection profile with its width of ∼14°. These data were measured on the CAD4 using a wavelength λ set at 0.75 Å during the measurement. This value was selected because it is close to the geometrical average in the Δλ window in the monochromated Mo beam.

4.1. The characteristic lines

The intensity distribution typical for the characteristic emission lines was modeled using a Lorentzian expression,

$$I(\lambda) = I(\alpha_1)\left[1 + 4\frac{(\lambda-\alpha_1)^2}{a_1^2}\right]^{-1} + I(\alpha_2)\left[1 + 4\frac{(\lambda-\alpha_2)^2}{a_2^2}\right]^{-1},$$

in which α_1 and α_2 are the wavelengths 0.70926 and 0.71354 Å of the Mo $K\alpha$ doublet. The widths of these peaks are represented by a_1 and a_2. Of course, the observed reflection profile (see Fig. 10) contains a broadened image of those sharp Lorentz peaks. The peak broadening is the logical consequence of the size of the analyzing Al_2O_3 crystal. We included its mean radius Δ in our calculations. The intensity distribution in the crystal image at the detector is given by $(\Delta^2 - x^2)$, in which x is a displacement away from the crystal center. When we measure the displacement x along θ, it is clear that the crystal radius can be expressed in terms of λ.

This leads to

$$f(\lambda) = \int_{-\Delta}^{+\Delta} \frac{(\Delta^2 - x^2)\,\mathrm{d}x}{1 + 4[(\lambda-\alpha+\Delta)/a]^2}.$$

With $v = 2[(\lambda-\alpha+\Delta)/a]$ and $x = (av/2) - (\lambda-\alpha)$, this expression becomes

$$f(\lambda) = \frac{a}{2}\int_{2(\lambda-\alpha-\Delta)/a}^{2(\lambda-\alpha+\Delta)/a} \Big\{[\Delta^2 + (a^2/4) - (\lambda-\alpha)^2] + va(\lambda-\alpha) - (1+v^2)(a^2/4)\Big\}(1+v^2)^{-1}\,\mathrm{d}v.$$

This can be rewritten as a sum of three integrals, $f(\lambda) = f_1(\lambda) + f_2(\lambda) + f_3(\lambda)$.

These can be evaluated separately.

$$f_1(\lambda) = \frac{a[\Delta^2 + (a^2/4) - (\lambda-\alpha)^2]}{2}\int_{2(\lambda-\alpha-\Delta)/a}^{2(\lambda-\alpha+\Delta)/a} \frac{\mathrm{d}v}{1+v^2}$$
$$= \frac{a[\Delta^2 + (a^2/4) - (\lambda-\alpha)^2]}{2}\Big\{\arctan[2(\lambda-\alpha+\Delta)/a] - \arctan[2(\lambda-\alpha-\Delta)/a]\Big\},$$

$$f_2(\lambda) = a^2\frac{(\lambda-\alpha)}{2}\int_{2(\lambda-\alpha-\Delta)/a}^{2(\lambda-\alpha+\Delta)/a} \frac{v\,\mathrm{d}v}{1+v^2}$$
$$= \frac{a^2(\lambda-\alpha)}{4}\int_{2(\lambda-\alpha-\Delta)/a}^{2(\lambda-\alpha+\Delta)/a} \frac{\mathrm{d}(1+v^2)}{1+v^2}$$
$$= \frac{a^2(\lambda-\alpha)}{4}\big(\ln\{1 + 4[(\lambda-\alpha+\Delta)/a]^2\} - \ln\{1 + 4[(\lambda-\alpha-\Delta)/a]^2\}\big),$$

$$f_3(\lambda) = +\frac{a^3}{8}\int_{2(\lambda-\alpha-\Delta)/a}^{2(\lambda-\alpha+\Delta)/a} \frac{-(1+v^2)\,\mathrm{d}v}{1+v^2}$$
$$= \frac{a^3}{8}\int_{2(\lambda-\alpha-\Delta)/a}^{2(\lambda-\alpha+\Delta)/a} -\mathrm{d}v = \frac{-a^2\Delta}{2}.$$

These equations enable us to refine the mean crystal radius Δ during the profile optimization.

The reference profile used in the fitting routine is itself an average over 100 individual profile scans. This makes it possible to calculate for each step i within that profile an experimental uncertainty s_i^2 and an average $\langle I_i\rangle$. In a Poisson distribution, variance and average have the same numerical value. As indicated in Fig. 10, the ratio of $s_i^2/\langle I_i\rangle$ is practically equal to 1 at all points in the spectral distribution where $\mathrm{d}I/\mathrm{d}\lambda$ is close to zero. This error distribution cannot be attributed to electrical instabilities with their direct impact on the X-ray intensity. If these were important, we would have seen different values for $s_i^2/\langle I_i\rangle$ at the α_1–α_2 maxima compared to the values in the low-intensity regions. The main determinant for the error distribution is the fluctuation in the instrumental position during the scan. We decided to include the angular uncertainties by the introduction of a Gaussian function in our model spectrum. This introduces a convolution integral, which was evaluated *via* a series expansion. We have (Abramowitz & Stegun, 1968)

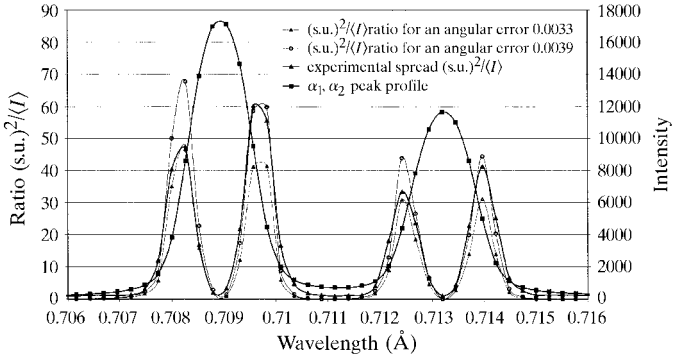

Figure 10
The $\alpha_1 - \alpha_2$ related profile of the Al_2O_3 reflection 6,3,18 at s = 1.2 Å^{-1}. We include its error distribution s_i^2/I_i caused by positional uncertainties. A Monte Carlo simulation with an angular error of 0.0035° reproduces the observed positional errors.

$$\int_{-\infty}^{+\infty} \exp(-x^2) f(x)\, \mathrm{d}x = \sum_{i=1}^{n} w_i f(x_i) + R_n$$

with

$$w_i = \frac{2^{n-1} n!\, \pi^{1/2}}{n^2 [H_{n-1}(x_i)]^2}, \qquad H_n(x_i) = 0$$

and

$$R_n = \frac{n!\, \pi^{1/2}}{2^n (2n)!}\, f^{(2n)}(\xi) \qquad (-\infty < \xi < +\infty).$$

H_n is the nth-order Hermite polynomial

The parameters (α_1, α_2, a_1, a_2, Δ) were obtained by least-squares fitting of the model profile to the observed one. The R value, defined as $[\Sigma(I_{\rm obs}-I_{\rm model})^2/\Sigma I_{\rm obs}]^{1/2}$, converged at 0.007.

The refined values for α_1 and α_2 were 0.7084 and 0.7127 Å. These numbers underestimate the tabulated values by 0.0009 Å. This discrepancy points to a systematic error. The wavelength axis in the observed profile is slightly shifted compared to the ideal axis through, most likely, a small inaccuracy in the experimental Al_2O_3 cell dimensions. The calculated a_1 and a_2 values indicate a FWHM of 0.00029 and 0.00033 Å for α_1 and α_2, respectively. These numbers are very close to the widths reported by Compton & Allison (1935). This shows that our model does indeed provide a proper description of the Mo $K\alpha$ emission lines.

The mean radius Δ of the analyzer crystal was also optimized. On the internal λ scale assigned to the reflection profile, we arrived at a value of 0.00088 Å. In the scan over 3.1° in ω (or θ), we covered a total wavelength window of 0.0245 Å. Thus, the radius of the crystal image projected by the X-ray beam on the detector has an angular width of 0.11° in θ. Given the 208 mm distance (Fig. 1) between the detector and the crystal position at the rotation axis, we calculated a crystal radius of 0.40 mm, *i.e.* the crystal image is about three times larger than the crystal itself. This discrepancy is easily accommodated *via* the beam divergence. We find a beam divergence of 0.09° as a result of the focal spot of 0.4 mm and the crystal radius of 0.15 mm. This leads at the detector to an expected crystal image with 0.47 mm radius. We find the agreement between observed and expected crystal size acceptable.

The Gaussian element in the profile description yields an s.u. value of 0.00014 Å, which corresponds to an angular uncertainty of 0.018°. We incorporated this σ value in a Monte Carlo simulation of profile scans. The resulting series of s^2/I values does not match the experimental values. The latter are much smaller than the former. This means that the real instrumental error has to be significantly smaller than 0.018°. Previous studies (Lenstra *et al.*, 1992) pointed at s.u. values of 0.003°. This value was verified using our Al_2O_3 profile scans. The angular s.u. margins were estimated by examining the distribution in the centers of gravity calculated for each scan. Intensities integrated over the applied scan angle are not affected by the angular error of 0.003°. This explains why counting statistics holds much better for the integrated measurements than for each step within the step/scan measurement.

Nevertheless, we have in Fig. 10 a situation in which Σs_i^2 exceeds by far $\Sigma\langle I_i\rangle$. This mismatch between the integrated intensity $\Sigma\langle I_i\rangle$ and its uncertainty, (s.u.)^2 = Σs_i^2, is caused by displacements of the peak profile within the scan window. The peak shift of 0.003° corresponds to 10% of the size of each step in the reflection scan. A peak displacement generates unavoidably related errors to be found at both sides of the true peak position. Therefore, Σs_i^2 exceeds the counting statistical error for the integrated intensity $\langle I\rangle$. The observed s.u. of 0.003° is the result of mechanical tolerance and instrumental friction. They come into play due to the design of the diffractometer. The rotations around ω and 2θ share the same axis. Mechanical tolerance is needed to accommodate independent movement of ω and 2θ. Unfortunately, a rotation of the detector arm (2θ) will introduce a small ω error as a result of friction. As shown previously by analyzing reflection profiles combining a positive and a negative scan direction (Lenstra *et al.*, 1992), the random error s.u., caused by friction, can become a systematic one. In such scans, the position difference between the centers of gravity reveals the systematic discrepancy caused by the fastest moving motor on the position controlled by the slave motor.

We introduced angular s.u. values of 0.0033 and 0.0039° in our Monte Carlo simulation. We find simulated uncertainties (s.u.)^2 that are practically equal to the observed s_i^2 values. The results of these simulations are included in Fig. 10.

We verified the robustness of our model for the α_1–α_2 spectrum using a second series of Al_2O_3 6,3,18 profile measurements. The data were collected with a tube voltage of 25 kV instead of the previously used value of 50 kV. $V_{\rm tube}$ controls the intensity ratio I(characteristic emission)/I(white continuum). At 25 kV, the Mo $K\alpha$ doublet is, on a relative scale, less dominant in the total beam intensity than at 50 kV (see §4.2 on the white continuum).

Nevertheless, we find no changes in the values of the optimized parameters for a_1, a_2, Δ and σ(Gauss).

4.2. White continuum

We measured the full spectrum of a graphite-monochromated Mo $K\alpha$ beam using the reflection 6,3,18 of Al_2O_3. Its profile was measured in an $\omega/2\theta$ scan mode over an angular range of 21° in ω (or θ). The center of each profile measurement was defined by λ = 0.75 Å. The profile scans were made using tube voltages of 50 and 25 kV. The variation in tube voltage makes it possible to separate the beam spectrum in the form of a coherent Bragg reflection from the local background intensity. The latter is polychromatic. The observed reflection profiles and the ratio I(25 kV)/I(50 kV) are shown in Fig. 11.

A shift in $V_{\rm tube}$ allows us to identify all three components, present in each profile. We have:

(i) The characteristic radiation. The α_1, α_2 intensity is proportional to $(V_{\rm tube} - V_{\rm exc})^{1.6}$ with $V_{\rm exc}$ = 20 kV, the excitation voltage of the Mo tube. Therefore, we expect for the

ratio $I(\alpha|25\ \mathrm{kV})/I(\alpha|50\ \mathrm{kV})$ a value of $\sim$0.06. This value corresponds well with the experimental result shown in Fig. 11.

(ii) The white continuum. The intensity $I(\lambda;$ *Bremsstrahlung*$)$ varies with $(V_{\rm tube}-V_\lambda)$. For a wavelength $\lambda \simeq 0.73$ Å, we have $V_\lambda = 12.398/0.73$ kV = 17 kV. Consequently, the variation in $V_{\rm tube}$ should lead to a value of 0.24 for $I(\lambda|25\ \mathrm{kV})/I(\lambda|50\ \mathrm{kV})$. We find that value close to $\lambda = 0.73$ Å in Fig. 11. Moving away from that point in the reflection profile, the intensity ratio decreases slowly to 0.09. This reduction is linked to the decrease in the elastic Bragg intensity, and it reflects the growing impact of the polychromatic background signal on $I(25\ \mathrm{kV})/I(50\ \mathrm{kV})$.

(iii) The background. Its response to a change in the tube voltage is determined by a weighted average over the behaviour of α_1, α_2 and of the white continuum. The typical value of the intensity ratio for the background is 0.09. This points to an incident X-ray beam with 13% intensity obtained from the tube's *Bremsstrahlung* and 87% intensity coming from the characteristic emission of the X-ray tube. This matches the result given in §2, where those percentages were obtained with the help of the X-ray transmission through a Y foil.

The intensity ratio of 0.09 in Fig. 11 identifies on both sides of the 6,3,18 reflection the local background. The beam spectra at 50 and 25 kV were inferred from the observed profiles employing a linear background interpolation. The 50 kV beam spectrum is presented in Fig. 12.

For the α_1 and α_2 emission lines, the model defined in §4.1 was used. Slightly different values for the wavelengths α_1 and α_2 and their intensities $I(\alpha_1)$ and $I(\alpha_2)$ were obtained due to the difference in the scan speed and in the mean wavelength (0.75 *versus* 0.71 Å) used. We expressed the spectral distribution of the white continuum as

$$I(\lambda) = \sum_{i=0}^{6} a_i\lambda^i + a_7/[1 + 4(\lambda - \lambda_w)^2/a_w^2].$$

The final parameter values are summarized in Table 1. The r.m.s. residual values converged at 0.002 and 0.004 for the data measured at 50 and 25 kV, respectively. The reduction in tube voltage reduces the integrated α_1 and α_2 intensity from 152 394 to 8166 counts. This variation matches our expectation based on $(V_{\rm tube} - 20)^{1.6}$. The expected shift in the intensity of the white continuum is a reduction by 1/4. Our model produces a change from 14 975 to 4939 counts, *i.e.* a reduction by 1/3. We believe that the discrepancy is linked to the complex issue of separating the monochromatic Bragg signal from the polychromatic background. The applied linear background interpolation is an oversimplification. The use of a background model such as described by Maes *et al.* (1998) should be advantageous. The same numbers show that the white continuum contribution to the total beam intensity is about 10% at 50 kV and it increases to 38% at 25 kV. The former number confirms the earlier estimates.

Table 1
Optimized spectral parameters.

	25 kV	50 kV
$a0$†	−221	−1120
$a1$†	892	4535
$a2$†	−1998	−10 187
$a3$†	2679	13 712
$a4$†	−2153	−11 060
$a5$†	959	4950
$a6$†	−183	−949
$a7$	469.5	1654.0
$I(\alpha1)$	28 053.7	522 993.2
$I(\alpha2)$	16 399.8	307 154.2
$\alpha1$	0.709365	0.709123
$\alpha2$	0.713641	0.713397
a_w	0.025924	0.024270
λ_w	0.716748	0.716370

† Parameters of the polynomial are multiplied by 10^{-6}.

5. Systematic intensity errors caused by spectral truncation

In the preceding section, we determined a model describing the spectrum in the X-ray beam to be used in a diffraction analysis. This spectral model is used to reconstruct the reflection profile as a function of the scattering angle θ. This profile characterizes a reflection observed along the $\omega/2\theta$ scan direction. The background–peak–background routine is applied to calculate the net intensity.

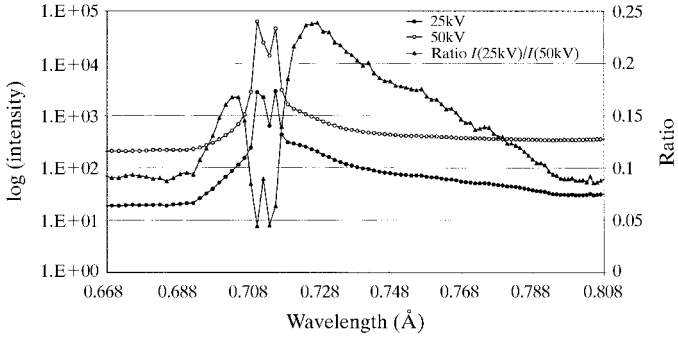

Figure 11
Identification of the characteristic radiation, the *Bremsstrahlung* and the incoherent background in the Al_2O_3 6,3,18 reflection scan *via* the intensity ratio $I(\lambda|25\ \mathrm{kV})/I(\lambda|50\ \mathrm{kV})$.

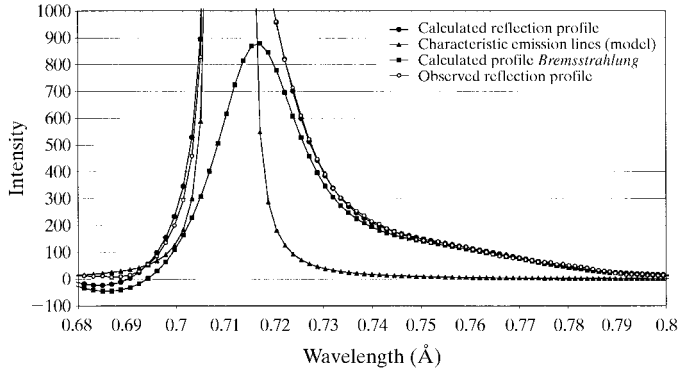

Figure 12
Observed and calculated intensity profiles of the 6,3,18 reflection of Al_2O_3. The calculated profile is the sum of a characteristic and a *Bremsstrahlung* component.

Table 2
The least-squares results of the refinements (on $|F|$) for oxalic acid.

FA model: 1158 reflections. LO model: 414 reflections. HO model: 744 reflections. N variables: 13 (x, y, z, B_{iso} per atom and the scale factor).

	Truncated						
	50 kV			25 kV			
	FA	LO	HO	FA	LO	HO	Untruncated
$\langle B \rangle$	0.0419 (5)	0.045 (1)	0.0314 (4)	0.1436 (6)	0.201 (2)	0.1168 (5)	0.00
Scale	0.164 (1)	0.163 (1)	0.165 (1)	0.183 (1)	0.179 (1)	0.186 (1)	0.158
R_1	0.006	0.004	0.005	0.011	0.010	0.006	0.004
R_w	0.016	0.011	0.013	0.019	0.014	0.014	0.004
S	3.12	2.23	2.52	3.56	2.84	2.67	0.23

The calculated reflection profile is adapted to a step-scan measurement. Each profile contains 96 steps measured along the $\omega/2\theta$ scan direction. The center of each scan is calculated using Bragg's law, $2d \sin\theta = \lambda$. In our profile analysis, $\lambda = (\alpha_1 + \alpha_2)/2$, *i.e.* the computational model uses the same wavelength as the experimental data collection (Enraf–Nonius, 1994). The scan width is defined by $(a + b \tan\theta)^\circ \times 1.5$. A uniform scan speed is employed. The integrated intensity over the central 64 steps represents the raw intensity R. The first and the last 16 steps are attributed to the local background B. This leads to a net intensity given by $I = R - 2B$.

In our model calculations, the background is absent, and thus a non-zero background points to the presence of a signal outside the central part of the scan. In an $\omega/2\theta$ scan mode, the spectral truncation error is visible twice, *viz* (i) the raw intensity underestimates the real intensity, and (ii) the local background overestimates the real background.

In Fig. 13(*a*), we show the result of our analysis for a scan width of $(1.3 + 0.4 \tan\theta)^\circ$. The calculations are made for the monochromated Mo $K\alpha$ beams generated with tube tensions of 50 and 25 kV. To complete our analysis, we omitted the $\alpha_1 - \alpha_2$ characteristic lines in the reflection shapes. This mimics the experiments in which a graphite monochromator is used to create an incident X-ray beam from the tube's white continuum only.

Fig. 13(*a*) is an almost perfect replica of Fig. 3 in a previous publication (Rousseau *et al.*, 2000). Consequently, our accurate analysis leads to an identical result, *viz* the truncation-error-induced bias in B ($= 8\pi^2 U$) of 0.05 and 0.22 Å^2 for tube tensions of 50 and 25 kV, respectively. These values are in line with the slopes of $\ln(I_{net}/I_{true})$ in Fig. 13(*a*). This model bias has been confirmed experimentally in the above-mentioned publication.

In this paper, we confine ourselves to a series of simulated experiments. A single molecule of oxalic acid was placed in a $5 \times 5 \times 5$ Å unit cell. The space group was $P\bar{1}$. Theoretical reflection intensities were calculated up to 1 Å^{-1} assuming a rigid structure ($B = 0$ Å^2) containing spherical atoms only.

In a first analysis, we used these intensities to refine the structure of oxalic acid. Reflections were weighted assuming $\sigma^2(I) = I$. The optimized structure model was in keeping with the original structure. The model was also robust, *i.e.* parameter values did not show any significant shift when we looked at models based on low-order (LO) data with $s < 0.7$ Å^{-1}, high-order (HO) data with $0.7 < s < 1.0$ Å^{-1} and full-angle (FA) data ($s < 1.0$ Å^{-1}). Here $s = \sin\theta/\lambda$.

We then introduced the truncation error typical for a scan angle of $(1.3 + 0.4 \tan\theta)^\circ$ and a tube tension of 50 kV. The results are shown in Table 2. We now find significant differences in the average B_{eq} values in the structure models (see Table 2). Thus ΔB (truncation) is in line with the above-mentioned value of 0.05 Å^2. Since the three refinement scenarios lead to significant discrepancies between the values

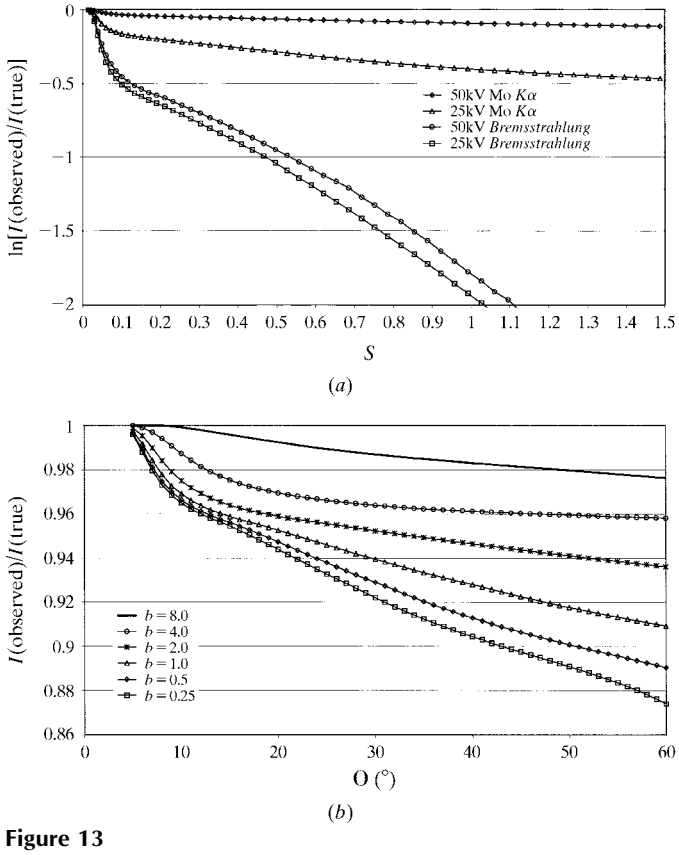

Figure 13
(*a*) The intensity truncation error as a function of the monochromaticity of the crystallographic X-ray beam obtained *via* a graphite monochromator. (*b*) The variation in the spectral truncation error as a function of the applied scan angle.

for B(model), the structure model lacks robustness due to spectral truncation.

The differences in B values become much larger when we introduce the truncation error typical for a tube tension of 25 kV. This choice results in B values shown in Table 2 for the FA, HO and LO models. It is clear that B(LO) is almost twice B(HO). This is exactly the opposite of that expected based on the treatment of truncation errors presented by Denne (1977). Relevant information on the least-squares results is included in Table 2. The variation in the scale-factor values is clearly visible in the 25 kV model calculations. Owing to the truncation error, we see that the LO data are ~8% more intense than the HO data. The remaining part of the truncation error is visible in the discrepancy between B(HO) and B(LO).

These model differences are in our opinion representative of the discrepancies often seen between HO and LO models while working on a study in deformation densities. The above-mentioned example makes it clear that those differences can be understood without any references to TDS effects or non-spherical electron densities.

The calculations with a monochromated white continuum beam result for 25 and 50 kV in different curves in Fig. 13(*a*). The 25 kV measurement shows the largest truncation errors. This is easily understood. In the white continuum, the intensity at $\lambda = 0.71$ Å is proportional to $(V_{\rm tube} - 17.5)$, whereas $I(\lambda = 0.79$ Å) is proportional to $(V_{\rm tube} - 15.7)$. Thus a reduction in tube voltage from 50 to 25 kV causes an asymmetric reduction in intensity. At $\lambda = 0.71$ Å, we find the largest reduction, *viz* from 1.0 to 0.23. At $\lambda = 0.79$ Å, the intensity decreases less, *viz* from 1.0 to 0.27. At higher θ values $I(0.79$ Å) is an element in the local background. This explains the increase in spectral truncation error as depicted in Fig. 13(*a*).

In Fig. 13(*b*), we depict the truncation error for measurements made with a tube tension of 50 kV using different scan widths $(a + b\tan\theta)^\circ$. Routine values for b are smaller than 1.0. For these scan ranges, we see the intensity truncation error starting at $\theta = 5^\circ$. The truncation error increases rapidly to 4%, which is reached at $\theta = 15^\circ$. Above $\theta = 15^\circ$, we see an almost linear decrease in the intensity $I_{\rm observed}$. Truncation errors of 10% are observed at $\theta = 45^\circ$ ($b = 0.25$) and $\theta = 50^\circ$ ($b = 0.5$)

6. Conclusions

The graphite monochromator with its mosaicity of 0.4 (1)° FWHM produces an X-ray beam with an almost homogeneous intensity distribution. This property makes the monochromated X-ray beam an attractive tool for X-ray diffractometry. Unfortunately, beam homogeneity is necessary, but not sufficient. Monochromaticity of the radiation in the beam is another requirement. For a graphite monochromator, the wavelength dispersion in the reflected X-ray beam depends heavily on the selected X-ray wavelength. The latter determines the X-ray absorption by the monochromator. μ varies with λ^3 and μ controls the *infinite* thickness of the monochromator. This element links the observed wavelength dispersion of 0.03 for a Cu $K\alpha$ beam with the $\Delta\lambda/\lambda$ value of 0.14 for a Mo $K\alpha$ beam. The latter value illustrates the poor performance of the monochromator. In the old days, accurate experiments involved the balanced filter technique. An Mo tube was combined with a Zr and a Y foil with $\lambda_{\rm abs}$ values of 0.688 and 0.728 Å, respectively. This led to intensity data based on a wavelength dispersion of 0.056. This suffices to show that the introduction of a monochromator is not necessarily a blessing.

The replacement of graphite(002) by Si(111) leads to monochromated X-ray beams with a wavelength dispersion of 0.03. For accurate analyses on small molecules, *e.g.* for a deformation study, this is acceptable, because it allows one to measure reflection intensities in the absence of spectral truncation errors. The increased monochromator absorption decreases its scattering volume and thus it reduces the overall intensity of the monochromated X-ray beam. The shift from graphite to silicon is at the expense of ~90% of the intensity. In addition, the Si(111)-monochromated X-ray beam is unattractive for a diffraction study, because the intensity distribution in the reflected X-ray beam is very inhomogeneous. The intensity pattern reflects the mass projection of the tube's filament on the anode. This intensity distribution at the focal spot is preserved in the X-ray beam due to the lack of mosaicity in the Si monochromator. Beam homogeneity can be improved by using larger foci. Unfortunately, this deteriorates $\Delta\lambda/\lambda$ *via* the beam divergence, which is determined by the size of the focus and the dimensions of the crystal to be analyzed.

Eliminating intensity errors caused by spectral truncation is from an experimental point of view clearly problematic. Beam homogeneity requires graphite instead of Si and thus every experiment with short wavelengths (*e.g.* $\lambda < 1$ Å) is hampered by systematic intensity truncation errors. We decided to correct those errors after the practical data collection itself had finished. This requires detailed knowledge regarding the spectrum of the radiation used in the diffraction experiment. In combination with the applied scan angle $[a + (\Delta\lambda/\lambda) \times (360/2\pi)\tan\theta]^\circ$ and for data measured along the $\omega/2\theta$ direction, *i.e.* a direction which parallels the wavelength axis, an intensity correction can be calculated and applied on the observed data set.

A complete beam spectrum was obtained by analyzing on the CAD4 diffractometer a high-order reflection of Al_2O_3 using a wavelength-dispersive measurement. The curve for Mo $K\alpha$ (50 kV) in Fig. 13(*a*) was used to eliminate the spectral truncation errors present in the CAD4 inferred data set of $NiSO_4{\cdot}6H_2O$. The optimized $B_{\rm eq}$ values of the non-H atoms increased by 0.04 Å^2. Thus, their untruncated values became practically equal to the $B_{\rm eq}$ values calculated using synchrotron data (Rousseau *et al.*, 2000).

The changes in the X-ray structure model caused by spectral truncation errors were analyzed using simulated experiments. When we compare the models refined using truncated and untruncated intensity data, we find B(truncated) > B(untruncated). The discrepancy between the two B values increases with the size of the truncation error.

Even in the absence of multiple data sets, it is possible to identify the presence of truncated data. HO and LO data lead

in the refinement to differences in the X-ray models. We find B(HO) < B(LO). This is in line with our experience. We also find a shift in scale factors. They show that I(LO) is more intense than I(HO). Thus the intensity loss caused by truncation is partly incorporated in the scale factor and partly in the ADPs. To analyze the spectral truncation errors, we used point-detector equipment. In collaboration with Utrecht University (Laboratorium voor Kristal en Structuurchemie), we performed some experiments using a CCD area detector. We found analogous model inconsistencies, *i.e.* variations in B_{eq} and scale factors. The model changes, caused by a variation in tube voltage only, were observed again. The lack of monochromaticity does affect the measurements made with a point detector. The intensity measurement *via* an area detector appears to be equally vulnerable.

APPENDIX *A*
Detector unit and its response function

Before we tackled the issue of monochromator-defined X-ray beams, it was necessary to look at the original tube spectra. For brevity, we confine ourselves to the measurements with a fine-focus Rh tube operated at 50 kV. This tube voltage defines the minimum X-ray wavelength in the tube spectrum *via* $\lambda = hc/eV$, which reduces to 12 398/V for a wavelength in Å. The pulse amplitude discrimination of the NaI detector unit was adjusted to the Rh $K\alpha$ radiation using the instructions given in the CAD4 manual (Schagen *et al.*, 1988). Window setting and high-voltage amplification were kept constant during the spectral analysis. The reflections $\bar{1}3\bar{3}$ and $\bar{2}6\bar{6}$ of the Si analyzer were both measured over 21° along the $\omega/2\theta$ scan direction. Given the Si symmetry, $I(\bar{2}6\bar{6})$ is a zero intensity. Its profile was measured because it represents the $\bar{1}3\bar{3}$ reflection for $\lambda > 1.1$ Å. The observed intensity profile is depicted in Fig. 14. Here, λ is calculated from θ using Bragg's law. The $K\alpha$ and $K\beta$ emission lines are clearly visible at 0.6147 and 0.5465 Å. The intensity ratio Rh-$K\beta$/Rh-$K\alpha$ is 0.18, which corresponds well with the tabulated value of 0.19. The intensities of the emission lines are superimposed upon the white continuum. Fig. 14 shows that the *Bremsstrahlung* reaches a maximum intensity at 0.615 Å. This observation is an artifact, but it is the logical consequence of the detector setting.

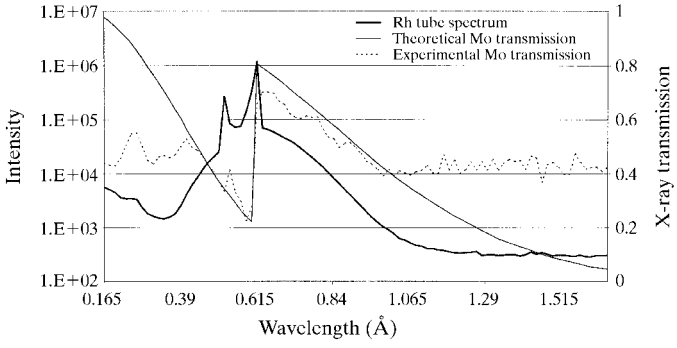

Figure 14
The spectrum of the Rh tube operated at 50 kV.

Theoretical spectra of X-ray tubes can be calculated (Pella *et al.*, 1985; Ebel *et al.*, 1989). For the white continuum we have Kramer's rule, *i.e.* the intensity I as a function of λ is proportional to (V_{tube} − 12398/λ). Thus, $I(\lambda)$ varies linearly with λ. The 'parabolic' intensity patterns around Rh $K\alpha$ in the observed spectrum (see Fig. 14) represent clearly a deformed picture of the real spectrum.

The deviation from linearity is caused by the response function of the detector with its fixed setting. The λ range, in which this response function is unequal to zero, could be determined with an Mo foil (λ_{abs} = 0.6198 Å). We inserted such a foil of thickness 0.02 mm just after the collimator, *i.e.* between the X-ray tube and the Si analyzer. The experimental transmission of X-rays through the foil is included in Fig. 14. The theoretical transmission as a function of λ was calculated using Victoreen's expression for the mass absorption coefficient (*International Tables for X-ray Crystallography*, 1968). We used $\mu/\rho = C\lambda^3 - D\lambda^4$. The constants C and D are tabulated per element and their values change abruptly at the absorption edge. Only for the experimental data with $0.4 < \lambda < 1.0$ Å do we find a reasonable agreement between the theoretical and the practical X-ray transmissions. Only this limited part of the total profile shows Bragg scattering because the relation between μ and λ holds. Outside this λ window, we observe an almost constant transmission of 0.4. This value apparently identifies the incoherent background signal with its wavelength distribution that is determined by the original tube spectrum. Thus with the Rh $K\alpha$ (photon energy of 20 keV) optimized detector setting, we observe a non-zero response from the detector for photon energies between 12 and 32 keV. Energy discrimination is clearly a weak point in the NaI detector entity. For the graphite-monochromated beam of Rh $K\alpha$, we have an energy window of 3 keV (see §2) in the beam compared to the detector-determined energy opening of 20 keV. This makes energy discrimination by the detector setting practically impossible while working with 'monochromated' X-ray beams.

At the Rh absorption edge (λ_{abs} = 0.543 Å), we see in Fig. 14 a discontinuity in the *Bremsstrahlung* intensity. In the absence of Rh absorption, we expect an almost equal intensity for wavelengths at both sides of the Rh absorption edge. The results in Fig. 14 suggest an intensity transmission of 0.3 just before the absorption edge. This X-ray transmission points to an optical path of 30 µm for the X-ray photons in the Rh anode. This path of 0.03 mm corresponds *via* the take-off angle of 6° to a photon production at a depth of 3 µm in the anode. This distance is apparently the average penetration depth of the 50 kV electrons in the anode.

References

Abramowitz, M. & Stegun, I. A. (1968). *Handbook of Mathematical Functions*, p. 890, formula 25.4.42. New York: Dover.
Arndt, U. W. & Wonacott, A. J. (1977). Editor. *The Rotation Method in Crystallography*. Amsterdam: North-Holland.
Blessing, R. H. (1987). *Crystallogr. Rev.* **1**, 3–58.

Compton, A. H. & Allison, S. K. (1935). *X-ray in Theory and Experiment*, 2nd ed., pp. 744–745. New York: Van Nostrand.
Denne, W. A. (1977). *Acta Cryst.* A**33**, 438–440.
Destro, R. & Marsh, R. E. (1987). *Acta Cryst.* A**43**, 711–718.
Destro, R. & Marsh, R. E. (1993). *Acta Cryst.* A**49**, 183–190.
Duisenberg, A. J. M. (1998). PhD thesis, State University of Utrecht, The Netherlands.
Ebel, H., Ebel, M. F., Wernisch, J., Poehn, Ch. & Wiederschwinger, H. (1989). *X-ray Spectrom.* **18**, 89–100.
Eisenstein, M. & Hirshfeld, F. L. (1983). *Acta Cryst.* B**39**, 61–75.
Enraf–Nonius (1994). *CAD4 Express Operations Manual.* Enraf–Nonius, Delft, The Netherlands.
Hirshfeld, F. L. & Hope, H. (1980). *Acta Cryst.* B**36**, 406–415.
International Tables for X-ray Crystallography (1968). Vol. III, §3.2. Birmingham: Kynoch Press.
Keulen, E. (1969). PhD thesis, State University of Groningen, The Netherlands.
Lenstra, A. T. H., Verbruggen, M., Bracke, B., Van Dijck, B., Vanhulle, C. & Vanhouteghem, X. (1992). *Bull. Soc. Chim. Belg.* **101**, 5–13.
Maes, S. T. (1997). PhD thesis, University of Antwerp (UIA), Belgium.
Maes, S. T., Vanhulle, C. & Lenstra, A. T. H. (1998). *Acta Cryst.* A**54**, 399–410.
Mathieson, A. McL. (1989). *Acta Cryst.* A**45**, 613–620.
Mathieson, A. McL. & Stevenson, A. W. (1996). *Crystallogr. Rev.* **6**, 59–155.
Pella, P. A., Feng, L. & Small, J. A. (1985). *X-ray Spectrom.* **14**, 125–135.
Rousseau, B., Maes, S. T. & Lenstra, A. T. H. (2000). *Acta Cryst.* A**56**, 300–307.
Ryan, T. W. (1986). PhD thesis, University of Edinburgh, Scotland.
Schagen, J. D., Straver, L., van Meurs, F. & Williams, G. (1988). *CAD4 Manual.* Enraf–Nonius, Delft, The Netherlands.